uc3m | Universidad Carlos III de Madrid

e-Archivo

This is a postprint version of the following published document:

Sánchez-Arriaga, G., Serrano-Iglesias, J. A., Leuthold, R. & Diehl, M. (2021). Modeling and Natural Mode Analysis of Tethered Multi-Aircraft Systems. *Journal of Guidance, Control, and Dynamics, 44*(6), 1199–1210.

DOI: 10.2514/1.g005075

© 2021 by the American Institute of Aeronautics and Astronautics, Inc.

Modeling and natural mode analysis of tethered multi-aircraft systems

Gonzalo Sánchez-Arriaga[1] and Jose Antonio Serrano-Iglesias[2]
Carlos III University of Madrid, Leganés, 28911, Spain

Rachel Leuthold[3] and Moritz Diehl[4]
University of Freiburg, Freiburg, D-79110, Germany

Two complementary simulators aimed at the dynamic analysis of airborne wind energy systems based on multi-aircraft configurations are presented. The first model considers a train of stacked aircraft linked among them by two inelastic and massless tethers with no aerodynamic drag. The architecture of the mechanical system in the second simulator is configurable, as long as the system is made of a set of aircraft linked by an arbitrary number of elastic tethers. In both cases, the aircraft are modeled as rigid bodies and the controller is incorporated in the aerodynamic torque through the deflections of control surfaces. An analysis of the symmetric equilibrium state and the corresponding natural modes of a train (stacked configuration) of aircraft was carried out. It revealed that the higher the position of the aircraft in the train, the more they participate in the modes. Tether inertial and aerodynamic drag effects increase the equilibrium angles of attack of the aircraft and the tether tension at the attachment points. The potential applications and computational performance of the two codes are discussed.

---

[1] Ramón y Cajal Fellow, Bioengineering and Aerospace Engineering Department, Avda. de la Universidad 30, 28911, Leganés, Madrid, Spain, gonzalo.sanchez@uc3m.es
[2] Aerospace Engineer, Bioengineering and Aerospace Engineering Department, Avda. de la Universidad 30, 28911, Leganés, Madrid, Spain.
[3] PhD student, Systems Control and Optimization Laboratory, Dept. of Microsystems Engineering & Dept. of Mathematics, University of Freiburg, Georges-Köhler-Allee 102, Freiburg, D-79110, Germany
[4] Full Professor, Systems Control and Optimization Laboratory, Dept. of Microsystems Engineering & Dept. of Mathematics, University of Freiburg, Georges-Köhler-Allee 102, Freiburg, D-79110, Germany

Nomenclature

A	= aircraft surface, m^2
b	= aircraft wingspan, m
c	= aircraft chord, m
C_{X0}, C_{Z0}, C_{m0}	= Aerodynamic coefficients
$C_{X\alpha}$, $C_{Y\beta}$, $C_{Z\alpha}$	= Aerodynamic force coefficients
$C_{m\alpha}$, $C_{l\beta}$, $C_{n\beta}$,	= Aerodynamic torque coefficients
C_{lp}, C_{mq}, C_{nr}	= Aerodynamic torque coefficients
D_t	= tether diameter, m
E_t	= tether Young modulus, Pa
$\tilde{\boldsymbol{e}}$	= eigenvector of the Jacobian matrix
$\boldsymbol{f}_A$	= normalized aerodynamic force
g	= gravitational acceleration, m/s^2
$\bar{\boldsymbol{J}}$	= Jacobian matrix
L	= tether length, m
L_0	= reference length, m
M	= mass of the aircraft, kg
$\boldsymbol{m}_A$	= normalized aerodynamic torque
N_K	= number of aircraft
N_P	= number of point-like masses
$\bar{\boldsymbol{R}}$	= rotation matrix
$\boldsymbol{r}$	= normalized position vector
$\boldsymbol{v}$	= normalized velocity vector
$\boldsymbol{\omega}$	= normalized angular velocity vector
$\boldsymbol{q}_s$	= vector of coordinates
$\bar{\boldsymbol{\iota}}_K$	= normalized tensor of inertia
$\boldsymbol{T}$	= tether tension, N
v_A	= normalized aerodynamic velocity
V_T	= reference velocity, m/s
$\boldsymbol{x}, \boldsymbol{y}, \boldsymbol{z}$	= unit vectors of a frame of reference

α = angle of attack, rad

β = sideslip angle, rad

ν_t = dimensionless friction coefficient

ρ = air density, kg/m^3

ρ_t = tether density, kg/m^3

τ = normalized time

φ, γ, θ, η = aircraft coordinates, rad

Subscripts

E = Earth

K = aircraft/kite

P = point-like mass

t = tether

Relevant geometric points

$D^{\pm}$ = down tether attachment point

G = center of mass of the aircraft

O = origin of frame of reference

$U^{\pm}$ = upper tether attachment point

I. Introduction

Systems made of several aircraft, such as airplanes, kites, and balloons, linked by tethers (or a hose in aerial refueling scenarios) appear in a wide range of scenarios and applications. Their modeling, dynamics and control constitute an engineering challenge in flight mechanics due to the coupling of the motion of the vehicles and the flexible tethers. A popular example in aerospace engineering is the aerial refueling of aircraft, whose dynamics and control has been recently tackled by a boundary control scheme based on a backstepping method [14]. Systems of tethered multicopters linked by inelastic [25] and elastic [8] tethers were also considered. Dragon kites, which are made of a series of kites in a train or stack, are part of Chinese folklore [12] and are among the most

beautiful man-made flying machines. The longest dragon kite flown in 2015 was made up of 2000 pieces with a total length of 6000 meters.

Recent work on airborne wind energy (AWE) shows that interest on multi-aircraft systems linked by tethers can grow in the near future because, although their technological readiness level is low as compared with other AWE concepts, their power scale assessment can reach around 10MW [26]. AWE systems harvest wind energy by using the tether traction to rotate a generator installed on the ground (ground-generation) or by using onboard wind turbines and transmitting the energy to the ground via a special rope (airborne-generation) [5, 23]. They operate at higher altitudes than conventional wind turbines, where winds are generally stronger and more persistent. This feature constitutes an important advantage because it has also been shown that accessing higher altitudes and dynamically adjusting the operation to the wind resource typically increase the available energy for 95% of the time by a factor of two as compared with fixed harvesting altitudes [2]. Several technology demonstrators are already available and studies on the challenges of their commercialization have been performed [6].

Multi-aircraft configurations can help AWE in different directions. For instance, a dual-airfoil design has been proposed to reduce the aerodynamic drag on the main tether [13, 16, 17, 28]. A kite network in a ring configuration has been also proposed [18]. On the other hand, most of AWE companies have scaled up their demonstrators to generate more power. However, such a strategy may be limited by mechanical constraints beyond a certain aircraft size. Switching to a configuration with several stacked aircraft can be an interesting alternative. Moreover, tether sagging would be reduced due to the tether tension enhancement. These important advantages apply to both airborne- and ground-generation systems. Since flight dynamics and stability of multi-aircraft configurations has been identified as two important topics for AWE community [26], this manuscript addresses the technical and theoretical challenge of developing efficient numerical tools to simulate the dynamics of several tens of aircraft linked by tethers and satisfying two key requirements. First, the aircraft should be modelled as rigid bodies (instead of point masses) in order to capture the attitude dynamics. Second, the tools should be flexible and provide diverse degree of fidelity and computational cost to assist the different phases of the design.

This work fulfilled the requirements by developing two models of different complexity (see Secs. II and III). A common feature, which also distinguishes them from previous studies, is that they both consider the longitudinal and lateral-directional dynamics of a generic number of aircraft modeled as rigid bodies. The first model simulates a train of aircraft linked by inelastic and very thin (massless and no aerodynamic drag) tethers. It implements a Lagrangian formulation with an approach based on minimal coordinates. Such a methodology has been commonly adopted for AWE systems because the fast longitudinal oscillations of the tethers are removed and the resulting set of ordinary differential equations is not coupled with algebraic constraints [15, 19, 22, 24, 27]. As compared with other approaches, this choice adds some technical difficulties and cumbersome calculations but it provides a non-stiff and efficient set of ordinary differential equations. These properties of our model are essential to address new scenarios involving tethered systems with a large number of aircraft (up to 20 in our calculations). An alternative approach, already used to model multi-aircraft systems in AWE [4], is using non-minimal coordinates and working with a mix system of differential and algebraic equations [11]. The second simulator considers a generic multi-aircraft configuration linked by elastic tethers and it retains tether inertial and aerodynamic drag effects. Following previous work [9, 10], the tethers are substituted by a chain of masses linked by springs and dampers. Besides presenting two complementary numerical tools to study the nonlinear dynamics of tethered multi-aircraft systems and a comparison among them, the main contribution and novelty of this work is the analysis of the natural modes of systems made of a large number of aircraft (see Sec. IV). The study also presents a periodic trajectory driven by an open-loop controller for a system made of five aircraft. The conclusions of the work are summarized in Sec. V. The two codes, named KiteTrain and KiteElastic, have been added as independent modules to the AWE software LAKSA, which is available in a public repository [21].

II. A train of aircraft linked by inelastic tethers

A. General description of the system

We first consider a train of N_k aircraft linked by $2N_k$ straight and inelastic tethers (see Fig.1). Due to its high complexity, some conventions and notations need to be introduced for clarity and

conciseness. For convenience, we will use a normalized time $\tau = t\sqrt{g/L_0}$, with g the gravitational acceleration and L_0 a reference length of the system. These two variables and the mass of the first aircraft M_K^1 will act as characteristic magnitudes to construct dimensionless variables and achieve a compact formulation of the equations of motion. For convenience, the sine and cosine of an angle α are denoted by $s\alpha$ and $c\alpha$. Bold style and bold style with a bar are used for vectors and matrices, respectively. Two capital letters with a bar on the top mean a vector with origin and tip at the points denoted by the capital letter. The unit vectors of a frame of reference are $\boldsymbol{x}$, $\boldsymbol{y}$ and $\boldsymbol{z}$.

The train of aircraft is attached to a fixed point O_E at the ground. Such a point is the origin of an inertial Earth-fixed frame with unit vectors $\boldsymbol{x}_E$ and $\boldsymbol{y}_E$ spanning the flat ground and $\boldsymbol{z}_E$ pointing downwards. For simplicity, it will be assumed that the wind is horizontal and blows opposite to $\boldsymbol{x}_E$. Among the different models proposed in the literature [1], we considered the following logarithmic wind shear model

$$\boldsymbol{V}_w = -V_{w0}(\tau)\frac{\ln\left(H/H_r\right)}{\ln\left(H_0/H_r\right)}\boldsymbol{x}_E \tag{1}$$

with $V_{w0}(\tau)$ a reference velocity that can contain non-stationary and stochastic disturbances, H_r a roughness factor, H_0 a reference altitude, and H the altitude.

Each aircraft labeled by a superscript i and with mass M_K^i, wingspan b_K^i, chord c_K^i, and surface A_K^i, will be considered to be a rigid body. For convenience, they are enumerated from $i = 1$ (the lowest) to $i = N_k$ (the uppermost). For each aircraft, we introduce a right-handed frame of reference S_K^i attached to it, origin at its center of mass G_i, and unit vectors $\boldsymbol{x}_K^i$ and $\boldsymbol{z}_K^i$ spanning the plane of symmetry of the aircraft. The S_K^i-component of the tensor of inertia of aircraft i about G_i is

$$\bar{\boldsymbol{I}}_K^i = M_K^1 L_0^2 \bar{\boldsymbol{\iota}}_K^i, \qquad \bar{\boldsymbol{\iota}}_K^i \equiv \begin{pmatrix} \iota_x^i & 0 & \iota_{xz}^i \\ 0 & \iota_y^i & 0 \\ \iota_{xz}^i & 0 & \iota_z^i \end{pmatrix} \tag{2}$$

with ι_x^i, ι_y^i, ι_z^i, and ι_{xz}^i some constants.

Each aircraft, except the one with index $i = N_K$, is linked to four tethers and has, consequently,

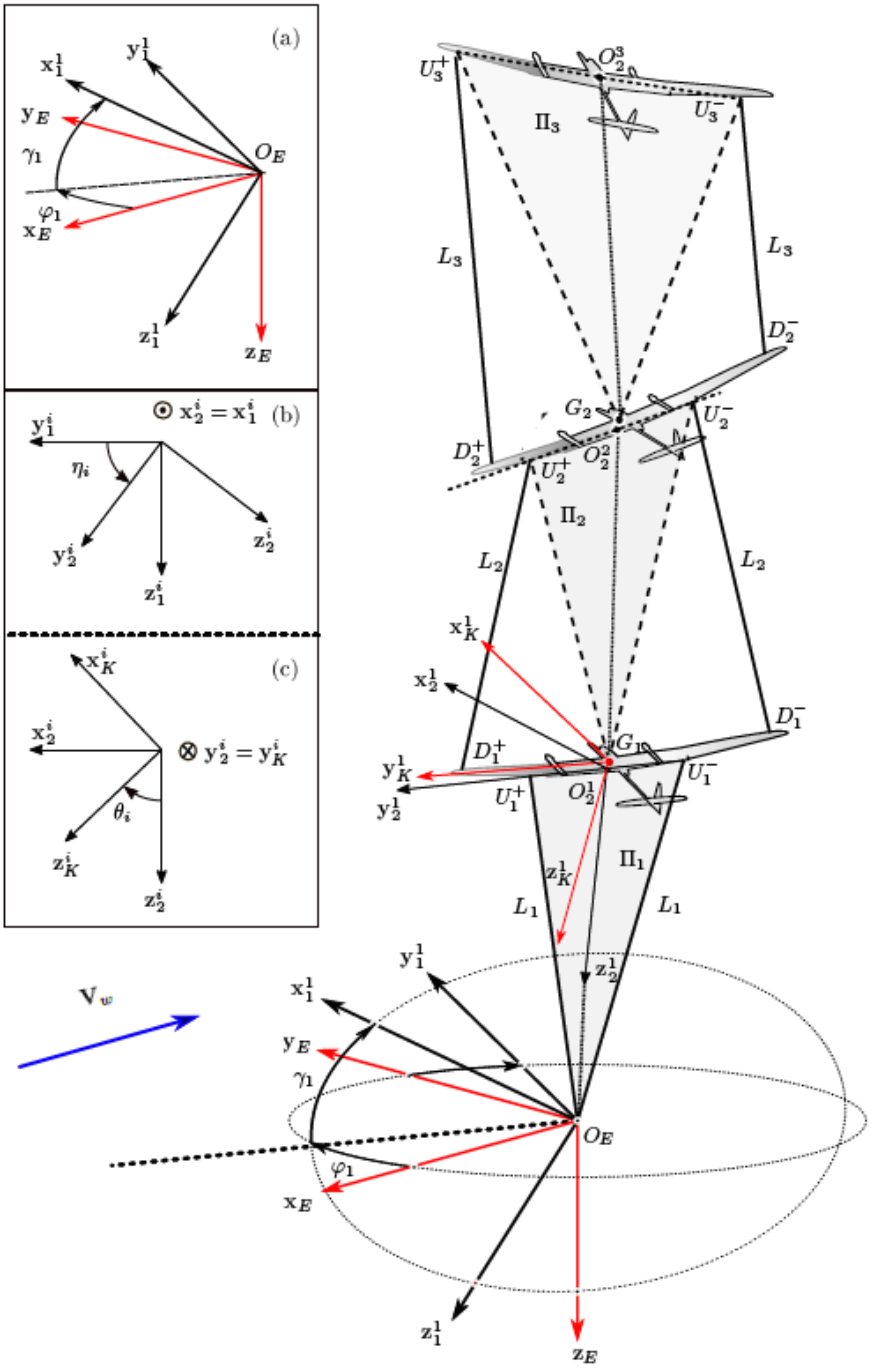

Fig. 1 Sketch of the train of aircraft, coordinates and frames of reference.

four attachment points. Let us call U_i^+ and U_i^- the points of aircraft i where the tethers that link it with aircraft number $i-1$ are attached. These points are placed symmetrically with respect to the plane of symmetry of the aircraft and they are fixed for an observer linked to the frame S_K^i. The same property holds for points D_i^+ and D_i^-, which are defined as the points of aircraft i where the

two tethers that link it with aircraft number $i+1$ are attached. The S_K^i-coordinates of the vectors with origin at G_i and tips at these four important points are

$$\overrightarrow{G_iU_i^{\pm}} = L_0 \left(x_U^i \boldsymbol{x}_K^i \pm y_U^i \boldsymbol{y}_K^i + z_U^i \boldsymbol{z}_K^i \right), \tag{3}$$

$$\overrightarrow{G_iD_i^{\pm}} = L_0 \left(x_D^i \boldsymbol{x}_K^i \pm y_D^i \boldsymbol{y}_K^i + z_D^i \boldsymbol{z}_K^i \right), \tag{4}$$

where x_U^i, y_U^i, z_U^i, x_D^i, y_D^i and z_D^i are six dimensionless constants that define the positions of the attachment points. According to this notation, the down and upper tips of a tether are named with letter D and U (see Fig. 1).

Regarding the tethers, we will assume that they are massless, inelastic, and straight. The lengths of the tethers are constant and symmetrically distributed. The aerodynamic drag is also ignored. These assumptions, which simplify the analysis notably, will be relaxed in Sec. III. Let us call L_i the length of the tether with tips at points U_i^+ and D_{i-1}^+ (or U_i^- and D_{i-1}^-). The same definition applies for L_1, except that points D_0^+ and D_0^- are replaced by the origin of the inertial frame, O_E.

B. Coordinates and auxiliary frames of reference

The straight and inelastic tether assumption suggests the use of a Lagrangian formulation with a minimal coordinate approach. By following such a strategy, the constraint forces introduced by the inelastic tethers, i.e. the tensions, will not appear explicitly in the equations of motion. However, the selection of the coordinates should be done carefully in order to keep the effort in the analytical calculations low. In general, a mechanical system made of N_k rigid aircraft has $6N_k$ degrees of freedom. Our train of aircraft, which also involves $2N_k$ geometrical constraints due to the inelastic tethers, has $6N_k - 2N_k = 4N_k$ degrees of freedom. We will gather all of them in the coordinate vector

$$\boldsymbol{q}_s = [\boldsymbol{q}_s^1 \;\; \boldsymbol{q}_s^2 \cdots \; \boldsymbol{q}_s^{N_k}]^T, \tag{5}$$

which contains the coordinates of each aircraft

$$\boldsymbol{q}_s^i = [\varphi_i \;\; \gamma_i \;\; \eta_i \;\; \theta_i]^T. \tag{6}$$

The four angles in Eq. (6) have been chosen by generalizing the analysis of Ref. [20], which includes a detailed discussion of their definitions and four dedicated figures to understand the physical meaning of these angles. For convenience, we provide again in the next few paragraphs the definitions of the angles and how they determine the position and attitude of the frames attached to the aircraft (S_K^i) with respect to the inertial frame (S_E).

For each aircraft, we introduce the plane Π_i that contains points U_i^+, U_i^-, and G_{i-1} (or point O_E for aircraft number 1). These planes are shown in Fig. 1. Angles φ_i and γ_i orientate the S_E frame with respect to a frame named S_1^i that is linked to the Π_i-plane. Frame S_1^i has the origin at G_{i-1}, unit vectors $\boldsymbol{z}_1^i$ and $\boldsymbol{y}_1^i$ spanning the Π_i-plane and $\boldsymbol{x}_1^i$ normal to it. For clarity, only one of such auxiliary frames (S_1^1) and two angles (φ_1 and γ_1) are shown in Fig. 1. A detail of the orientation of a generic S_1^i frame is shown in inset (a), where for clarity the S_E frame was translated to make its origin coincident with point G_{i-1}. The rotation matrix that relates vector components in the S_E and S_1^i frame is

$$\bar{\boldsymbol{R}}_{1E}^i(\varphi_i, \gamma_i) = \begin{pmatrix} c\gamma_i c\varphi_i & c\gamma_i s\varphi_i & -s\gamma_i \\ -s\varphi_i & c\varphi_i & 0 \\ s\gamma_i c\varphi_i & s\gamma_i s\varphi_i & c\gamma_i \end{pmatrix}. \tag{7}$$

The angular velocity of frame S_1^i with respect to S_E is $\boldsymbol{\Omega}_{1E}^i = \sqrt{g/L_0}\boldsymbol{\omega}_{1E}^i$ with $\boldsymbol{\omega}_{1E} = \dot{\varphi}\boldsymbol{z}_E + \dot{\gamma}\boldsymbol{y}_1$ and the dot denotes the derivative with respect to the normalized time τ.

Angle η_i in Eq. (6) orientates frame S_1^i with respect to another auxiliary frame named S_2^i. It has origin O_2^i at the middle point of the segment $\overline{U_i^+ U_i^-}$, unit vector $\boldsymbol{x}_2^i$ is normal to the Π_i-plane and $\boldsymbol{y}_2^i$ points from U_i^- to U_i^+ (parallel to $\boldsymbol{y}_K^i$). After calling η_i the angle between $\boldsymbol{y}_1^i$ and $\boldsymbol{y}_2^i$ [see

inset (b) in Fig. 1], the rotation matrix $\bar{\boldsymbol{R}}^i_{21}$ that transforms vector components from S^i_1 to S^i_2 is

$$\bar{\boldsymbol{R}}^i_{21}(\eta_i) = \begin{pmatrix} 1 & 0 & 0 \\ 0 & c\eta_i & s\eta_i \\ 0 & -s\eta_i & c\eta_i \end{pmatrix}. \tag{8}$$

The angular velocity of S^i_2 with respect to S^i_1 is $\boldsymbol{\Omega}^i_{21} = \sqrt{g/L_0}\boldsymbol{\omega}^i_{21}$, where $\boldsymbol{\omega}^i_{21} = \dot{\eta}\boldsymbol{x}^i_2$.

Finally, since $\boldsymbol{y}^i_2$ and $\boldsymbol{y}^i_K$ are parallel, the relative orientation of frames S^i_2 and S^i_K is given by one angle. According to inset (c) in Fig. 1, let us call θ_i the angle between $\boldsymbol{x}^i_K$ and $\boldsymbol{x}^i_2$ and introduce the rotation matrix

$$\bar{\boldsymbol{R}}^i_{K2}(\theta_i) = \begin{pmatrix} c\theta_i & 0 & -s\theta_i \\ 0 & 1 & 0 \\ s\theta_i & 0 & c\theta_i \end{pmatrix}. \tag{9}$$

The angular velocity of S^i_K with respect to S^i_2 is $\boldsymbol{\Omega}^i_{K2} = \sqrt{g/L_0}\boldsymbol{\omega}^i_{K2}$ and $\boldsymbol{\omega}^i_{K2} = \dot{\theta}\boldsymbol{y}^i_K$.

C. Kinematic calculations

The construction of the Lagrangian function of the system involves some kinematic calculations, such as the angular velocities of the aircraft and the positions and velocities of their centers of mass. The computation of the normalized angular velocity of aircraft i with respect to S_E, which reads $\boldsymbol{\omega}^i_{KE} = \boldsymbol{\omega}^i_{K2} + \boldsymbol{\omega}^i_{21} + \boldsymbol{\omega}^i_{1E}$, is simple thanks to our choice of coordinates. Its S^i_K-components, $\boldsymbol{\omega}^i_{KE} = \omega^i_x\boldsymbol{x}^i_K + \omega^i_y\boldsymbol{y}^i_K + \omega^i_z\boldsymbol{z}^i_K$ are given by

$$\begin{pmatrix} \omega^i_x \\ \omega^i_y \\ \omega^i_z \end{pmatrix} = \bar{\boldsymbol{\Phi}}^i(\varphi_i, \gamma_i, \eta_i, \theta_i)\,\dot{\boldsymbol{q}}_s, \qquad i = 1 \cdots N_K \tag{10}$$

where all the elements of $\bar{\mathbf{\Phi}}^i$, which is a $3 \times 4N_k$ matrix, are equal to zero except

$$\bar{\mathbf{\Phi}}^i\left(1:3, 4(i-1)+1:4i\right) = \begin{pmatrix} -c\gamma_i c\eta_i s\theta_i - s\gamma_i c\theta_i & s\eta_i s\theta_i & c\theta_i & 0 \\ c\gamma_i s\eta_i & c\eta_i & 0 & 1 \\ c\gamma_i c\eta_i c\theta_i - s\gamma_i s\theta_i & -s\eta_i c\theta_i & s\theta_i & 0 \end{pmatrix}, \tag{11}$$

where the symbol $a:b$ denotes that the indices of the row (or the column) run from a to b.

The calculation of the normalized position ($\boldsymbol{r}_i$) and velocity ($\boldsymbol{v}_i$) vectors of the center of mass of aircraft number i is a bit cumbersome. The former is given by

$$\boldsymbol{r}_i \equiv \frac{\overline{O_E G_i}}{L_0} = \boldsymbol{r}_{i-1} - \frac{\overline{O_2^i G_{i-1}}}{L_0} + \frac{\overline{O_2^i G_i}}{L_0}, \tag{12}$$

where $\boldsymbol{r}_0$ is the null vector. Since vector $\overline{O_2^i G_{i-1}}$ belongs to the Π_i plane, we can write it as $\overline{O_2^i G_{i-1}}/L_0 = \zeta_i \boldsymbol{y}_2^i + \xi_i \boldsymbol{z}_2^i$ with ζ_i and ξ_i some constants to be determined afterwards. On the other hand, $\overline{O_2^i G_i}$ just depends on the coordinates of the attachments points. One readily verifies that

$$\boldsymbol{r}_i = \boldsymbol{r}_{i-1} - \left(\zeta_i \boldsymbol{y}_2^i + \xi_i \boldsymbol{z}_2^i\right) - \left(x_U^i \boldsymbol{x}_K^i + z_U^i \boldsymbol{z}_K^i\right). \tag{13}$$

Constants ζ_i and ξ_i are determined by using the constraints imposed by the inextensible tethers. First, we define the normalized length $\ell_i \equiv L_i/L_0$ and write the two constraints imposed by the two tethers of length L_i as

$$\ell_i \equiv \frac{|\,\overline{D_{i-1}^{\pm} U_i^{\pm}}\,|}{L_0} = \frac{|\,-\overline{G_{i-1} D_{i-1}^{\pm}} + \overline{G_{i-1} O_2^i} + \overline{O_2^i U_i^{\pm}}\,|}{L_0}. \tag{14}$$

Second, we note that $(\overline{O_2^i U_i^{\pm}} - \overline{G_{i-1} D_{i-1}^{\pm}})/L_0 = C_{xi}^{\pm} \boldsymbol{x}_2^i + C_{yi}^{\pm} \boldsymbol{y}_2^i + C_{zi}^{\pm} \boldsymbol{z}_2^i$ with

$$\begin{pmatrix} C_{xi}^{\pm} \\ C_{yi}^{\pm} \\ C_{zi}^{\pm} \end{pmatrix} = \pm \begin{pmatrix} 0 \\ y_U^i \\ 0 \end{pmatrix} - \bar{\boldsymbol{R}}_{2E}^i \bar{\boldsymbol{R}}_{EK}^{i-1} \begin{pmatrix} +x_D^{i-1} \\ \pm y_D^{i-1} \\ +z_D^{i-1} \end{pmatrix}, \tag{15}$$

$x_D^0 = y_D^0 = z_D^0 = 0$, and $\bar{\boldsymbol{R}}_{EK}^{i-1} \equiv \left(\bar{\boldsymbol{R}}_{K2}^{i-1}\bar{\boldsymbol{R}}_{21}^{i-1}\bar{\boldsymbol{R}}_{1E}^{i-1}\right)^T$. The two constraints in Eq. (14) then become

$$\ell_i^2 - C_{xi}^{\pm 2} \equiv \kappa_{i\pm}^2 = \left(\zeta_i - C_{yi}^{\pm}\right)^2 + \left(\xi_i - C_{zi}^{\pm}\right)^2. \tag{16}$$

These are the equations of two circumferences that belong to the Π_i-planes. They can be solved to find the following explicit form of ζ_i and ξ_i as a function of the coordinates

$$\begin{aligned}(\zeta_i, \xi_i) =& \frac{1}{2}\left(C_{yi}^+ + C_{yi}^-, C_{zi}^+ + C_{zi}^-\right) \\ &+ \frac{\kappa_{i+}^2 - \kappa_{i-}^2}{2R^2}\left(C_{yi}^- - C_{yi}^+, C_{zi}^- - C_{zi}^+\right) \\ &+ \frac{\Lambda}{2R^2}\left(C_{zi}^- - C_{zi}^+, C_{yi}^+ - C_{yi}^-\right)\end{aligned} \tag{17}$$

with

$$R \equiv \sqrt{\left(C_{yi}^+ - C_{yi}^-\right)^2 + \left(C_{zi}^+ - C_{zi}^-\right)^2} \tag{18}$$

$$\Lambda \equiv \sqrt{\left[\left(\kappa_{i+} + \kappa_{i-}\right)^2 - R^2\right]\left[R^2 - \left(\kappa_{i+} - \kappa_{i-}\right)^2\right]}. \tag{19}$$

The substitution of Eq. (17) in Eq. (A1), which is a more elaborated version of Eq. (13) given in Appendix A, provides the position vector of the center of mass of an aircraft as a function of the coordinates of the system, i.e. vector $\boldsymbol{q}_s$ defined in Eq. (5).

The velocity vector of the centers of mass are obtained by taking the τ-derivative of Eq. (A1). The S_E-components of the normalized velocity of aircraft i, $\boldsymbol{v}_i = v_x^i \boldsymbol{x}_E + v_y^i \boldsymbol{y}_E + v_z^i \boldsymbol{z}_E$, are

$$\begin{aligned}\begin{pmatrix} v_x^i \\ v_y^i \\ v_z^i \end{pmatrix} =& \begin{pmatrix} v_x^{i-1} \\ v_y^{i-1} \\ v_z^{i-1} \end{pmatrix} + \bar{\boldsymbol{\Xi}}\left(\varphi_i, \gamma_i, \eta_i, \theta_i, \xi_i, \eta_i, x_{Ai}, z_{Ai}\right)\dot{\boldsymbol{q}}_s^i \\ &+ \bar{\boldsymbol{X}}\left(\varphi_i, \gamma_i, \eta_i, \xi_i, \eta_i\right)\dot{\boldsymbol{q}}_s \equiv \bar{\boldsymbol{\Upsilon}}^i\left(\boldsymbol{q}_s\right)\dot{\boldsymbol{q}}_s\end{aligned} \tag{20}$$

where the explicit form of tensors $\bar{\boldsymbol{\Xi}}$ and $\bar{\boldsymbol{X}}_i$ are given in Appendix A. Tensor $\bar{\boldsymbol{\Upsilon}}^i$, which is a $3 \times 4N_k$ matrix, can be easily obtained from them.

It is important to note that, for $C^+_{yi} = C^-_{yi}$ and $C^+_{zi} = C^-_{zi}$, Eq. (17) is singular ($R = 0$). Such a situation happens for very particular configurations. For instance, when the attachment points are selected to have coordinates satisfying $y^i_U = y^{i-1}_D$ [see Eq. (3) and (4)] and simultaneously the dynamic state gives $\boldsymbol{y}^i_K = \boldsymbol{y}^{i-1}_K$. The physical reason behind such a singularity is that, for such special configuration, our choice of coordinates do not determine unambiguously the position of aircraft i. From a practical point of view, the singularity is not a problem because any difference between y^i_U and y^{i-1}_D, even if small, remove it. This issue of our choice of coordinates is compensated by the compactness of the formulation and the separation of longitudinal and lateral-directional modes (see Sec. IV A). In Sec. IV we avoided the singularity by considering a train of aircraft with $Y_U \neq Y_D$ for all the aircraft (see parameters in Table 1).

D. Equations of motion

Calling q_{sm} the m-component of the vector of coordinates in Eq. (5) ($m = 1 \dots 4N_K$), Lagrange's equations read [3]

$$\frac{\mathrm{d}}{\mathrm{d}\tau}\left(\frac{\partial \mathcal{L}}{\partial \dot{q}_{sm}}\right) - \frac{\partial \mathcal{L}}{\partial q_{sm}} = Q_m, \qquad m = 1, \dots, 4N_k. \tag{21}$$

with $\mathcal{L} = e_k - e_p$ the Lagrangian function, which includes the normalized kinetic and potential energies, and Q_m the normalized generalized forces. The kinetic energy of the system normalized over $M^1_K g L_0$ reads

$$e_k = \sum_{i=1}^{N_k}\left(\frac{1}{2}\sigma_i \boldsymbol{v}_i^T \cdot \boldsymbol{v}_i + \frac{1}{2}\boldsymbol{\omega}^{iT}_{KE}\bar{\boldsymbol{\iota}}^i_K \boldsymbol{\omega}^i_{KE}\right) = \frac{1}{2}\dot{\boldsymbol{q}}_s^T \bar{\boldsymbol{M}}\dot{\boldsymbol{q}}_s \tag{22}$$

where $\sigma_i = M^i_K / M^1_K$ and, from Eqs. (10) and (20),

$$\bar{\boldsymbol{M}} = \sum_{i=1}^{N_k}\left(\sigma_i \bar{\boldsymbol{\Upsilon}}_i^T \bar{\boldsymbol{\Upsilon}}_i + \bar{\boldsymbol{\Phi}}_i^T \bar{\boldsymbol{\iota}}^i_K \bar{\boldsymbol{\Phi}}_i\right). \tag{23}$$

Similarly, the normalized potential energy is

$$e_p(\boldsymbol{x}_s) = -\sum_{i=1}^{N_k} \sigma_i \boldsymbol{r}_i \cdot \boldsymbol{z}_E. \tag{24}$$

The generalized forces in Eq. (21) involves the aerodynamic force but not the tether tensions because the constraints are holonomic. The generalized force is [3]

$$Q_m = \sum_{i=1}^{N_k} \left(\boldsymbol{f}_A^i \cdot \frac{\partial \boldsymbol{v}_i}{\partial \dot{q}_{sm}} + \boldsymbol{m}_A^i \cdot \frac{\partial \boldsymbol{\omega}_{KE}^i}{\partial \dot{q}_{sm}} \right), \quad m = 1, \ldots, 4N_k. \tag{25}$$

In order to complete the dynamical system, it is necessary to introduce models for the normalized aerodynamic force, $\boldsymbol{f}_A^i$, and torque about G_i, $\boldsymbol{m}_A^i$, acting on aircraft i. We will use the simple model already implemented in previous airborne wind energy simulators and write the S_K^i-components of the aerodynamic force as

$$\begin{aligned} \boldsymbol{f}_A^i =& \mu_i v_{Ai}^2 \left[\left(C_{x0} + C_{x\alpha} \alpha_i \right) \boldsymbol{x}_K^i + C_{y\beta} \beta_i \boldsymbol{y}_K^i + \right. \\ & \left. \left(C_{z0} + C_{z\alpha} \alpha_i \right) \boldsymbol{z}_K^i \right], \end{aligned} \tag{26}$$

$$\begin{aligned} \boldsymbol{m}_A^i =& \mu_i v_{Ai}^2 \epsilon_b^i \left[\left(C_{l\beta} \beta_i + C_{lp} p_i + C_{l\delta_a} \delta_a^i \right) \boldsymbol{x}_K^i + \left(C_{n\beta} \beta_i + C_{nr} r_i + C_{n\delta_r} \delta_r^i \right) \boldsymbol{z}_K^i \right] \\ & + \mu_i v_{Ai}^2 \epsilon_c^i \left(C_{m0} + C_{m\alpha} \alpha_i + C_{mq} q_i + C_{m\delta_e} \delta_e^i \right) \boldsymbol{y}_K^i, \end{aligned} \tag{27}$$

with $\boldsymbol{v}_{Ai} = \boldsymbol{v}_i - \boldsymbol{V}_w / \sqrt{gL_0}$ the aerodynamic velocity, $\mu_i \equiv \rho A_K^i L_0 / 2M_K^1$, $\epsilon_b^i = b_K^i / L_0$, $\epsilon_c^i = c_K^i / L_0$, $(p_i, q_i, r_i) = \sqrt{g/L_0}(b_K^i \omega_x^i / 2, c_K^i \omega_y^i, b_K^i \omega_z^i / 2) / V_T$, ρ the air density, and V_T a reference velocity. All the coefficients in Eqs. (26)-(27), such as C_{x0}, $C_{x\alpha}$, $C_{l\beta}$, etc., are stability derivatives and depend on the shape of the aircraft [7]. The attack and sideslip angles are given by

$$\alpha_i = \arctan\left(\frac{\boldsymbol{v}_{Ai} \cdot \boldsymbol{z}_K^i}{\boldsymbol{v}_{Ai} \cdot \boldsymbol{x}_K^i} \right), \quad \beta_i = \arcsin\left(\frac{\boldsymbol{v}_{Ai} \cdot \boldsymbol{y}_K^i}{|\boldsymbol{v}_{Ai}|} \right). \tag{28}$$

Equation 27 also incorporates the torques generated by the deflections of some control surfaces like elevators (δ_e^i), ailerons (δ_a^i), and the rudders (δ_r^i).

Using previous results, Eq. (21) becomes

$$M_{ij}\ddot{q}_{sj} + \frac{\partial M_{ij}}{\partial q_{sk}}\dot{q}_{sk}\dot{q}_{sj} - \frac{1}{2}\frac{\partial M_{jk}}{\partial q_{si}}\dot{q}_{sj}\dot{q}_{sk} + \frac{\partial e_p}{\partial q_{si}} = \sum_{s=1}^{N_k}\left(f_{Al}^s \Upsilon_{li}^s + m_{Al}^s \Phi_{li}^s\right) \tag{29}$$

where $i = 1 \cdots 4N_K$, and Einstein's summation convention was used for the indices $k = 1 \ldots 4N_K$, $j = 1 \ldots 4N_K$ and $l = 1 \ldots 3$. In Eq. (29), f_{Al}^s and m_{Al}^s are the S_E- and S_K^s-components of vectors $\boldsymbol{f}_A^s$ and $\boldsymbol{m}_A^s$, respectively. Note that Eq. (26) gives the S_K^i components of the aerodynamic force and the rotation matrix $\bar{\boldsymbol{R}}_{KE}^i = \bar{\boldsymbol{R}}_{K2}^i \bar{\boldsymbol{R}}_{21}^i \bar{\boldsymbol{R}}_{1E}^i$ should be used to find the S_E-components, i.e. f_{Al}^s in Eq. (29). The set of equations given by (29) govern the dynamics of a train of aircraft linked by inelastic tethers. They have been implemented in the open-source code *LAKSA* under the module with name *KiteTrain*.

III. A train of aircraft linked by elastic tethers

Tether inertia, weight, flexibility, elasticity and aerodynamic drag have been all ignored in Sec. II, but they can be important in certain scenarios and configurations. For instance, these effects should be included to capture tether sagging in very long tethers. This section presents a high-fidelity model for a train of aircraft linked by an arbitrary number of elastic tethers. The code is also available in the open-source software *LAKSA* under the module with name *KiteElastic*.

A. Equations of motion of the aircraft

The model considers N_K aircraft linked among them by an arbitrary number of elastic tethers. Just two different types of frames are needed: (i) the inertial frame S_E and (ii) the frames S_K^i with origin at the centers of masses of the aircraft and linked to them. Regarding coordinates, since there are no geometrical constraints, the choice is much simpler now. The position and velocity vectors of the center of mass of aircraft i are written as $\boldsymbol{R}_i \equiv L_0 \boldsymbol{r}_i = L_0 \left(x_i \boldsymbol{x}_E + y_i \boldsymbol{y}_E + z_i \boldsymbol{z}_E\right)$ and $\boldsymbol{V}_i \equiv \sqrt{gL_0}\boldsymbol{v}_i = \sqrt{gL_0}\left(u_i \boldsymbol{x}_K^i + v_i \boldsymbol{y}_K^i + w_i \boldsymbol{z}_K^i\right)$. The attitude of each aircraft with respect to the inertial frame is given by the roll (ϕ_i), pitch (θ_i), and yaw (ψ_i) angles (find precise definitions and figures in [7]). These angles appear naturally in the rotation matrix that relates vector components

in the S_E and S_K^i frames

$$\bar{\boldsymbol{R}}_{KE}^i = \begin{pmatrix} c\psi c\theta & s\psi c\theta & -s\theta \\ c\psi s\theta s\phi - s\psi c\phi & s\psi s\theta s\phi + c\psi c\phi & c\theta s\phi \\ c\psi s\theta c\phi + s\psi s\phi & s\psi s\theta\cos\phi - c\psi s\phi & c\theta c\phi \end{pmatrix}, \tag{30}$$

where for brevity we omitted the subscript i in the angles. The absolute angular velocity of aircraft i is $\boldsymbol{\Omega}_{KE}^i \equiv \sqrt{\frac{g}{L_0}}\boldsymbol{\omega}_{KE}^i = \sqrt{\frac{g}{L_0}}\left(\omega_x^i \boldsymbol{x}_K^i + \omega_y^i \boldsymbol{y}_K^i + \omega_z^i \boldsymbol{z}_K^i\right)$.

Following the notation of Sec. II, we call U and D to the aircraft's points where the uppermost and lowermost tips of the tethers are attached. Similarly to Eqs. (3)-(4), the S_K^i-coordinates of these attachment points are

$$\overline{G_i U_i^m} = L_0\left(x_U^{im}\boldsymbol{x}_K^i \pm y_U^{im}\boldsymbol{y}_K^i + z_U^{im}\boldsymbol{z}_K^i\right), \tag{31}$$

$$\overline{G_i D_i^n} = L_0\left(x_D^{in}\boldsymbol{x}_K^i \pm y_D^{in}\boldsymbol{y}_K^i + z_D^{in}\boldsymbol{z}_K^i\right) \tag{32}$$

with index $i = 1\cdots N_K$ denoting the label of the aircraft and indexes $m = 1\cdots N_U^i$ and $n = 1\cdots N_D^i$ the number of attachment points of type U and D, respectively. Obviously, the relation $N_U^i = N_D^{i-1}$ holds and, for the example of Fig. 1, we have $N_U^i = N_D^i = 2$ for $i < 3$ and $N_U^3 = 2$ and $N_D^3 = 0$.

By using this notation, the equations of motions of the aircraft read

$$\frac{d}{d\tau}\begin{pmatrix} x_i \\ y_i \\ z_i \end{pmatrix} = \left(\bar{\boldsymbol{R}}^i_{KE}\right)^T \begin{pmatrix} u_i \\ v_i \\ w_i \end{pmatrix}, \tag{33}$$

$$\begin{aligned}\frac{d}{d\tau}\begin{pmatrix} u_i \\ v_i \\ w_i \end{pmatrix} =& \bar{\boldsymbol{R}}^i_{KE}\begin{pmatrix} 0 \\ 0 \\ 1 \end{pmatrix} - \boldsymbol{\omega}^i_{KE}\times\boldsymbol{v}_i \\ &+\frac{1}{\sigma_i}\left(\boldsymbol{f}^i_A + \sum_{m=1}^{N^i_U}\boldsymbol{f}_{U,im} + \sum_{n=1}^{N^i_D}\boldsymbol{f}_{D,in}\right),\end{aligned} \tag{34}$$

$$\frac{d}{d\tau}\begin{pmatrix} \phi_i \\ \theta_i \\ \psi_i \end{pmatrix} = \begin{pmatrix} \omega^i_x + \left(\omega^i_y s\phi_i + \omega^i_z c\phi_i\right) s\theta_i/c\theta_i \\ \omega^i_y c\phi_i - \omega^i_z s\phi_i \\ \left(\omega^i_y s\phi_i + \omega^i_z c\phi_i\right)/c\theta_i \end{pmatrix}, \tag{35}$$

$$\frac{d}{d\tau}\begin{pmatrix} p_i \\ q_i \\ r_i \end{pmatrix} = \left(\bar{\boldsymbol{\iota}}^i_K\right)^{-1}\left[\boldsymbol{m}^i_A - \boldsymbol{\omega}^i_{KE}\times\left(\bar{\boldsymbol{\iota}}^i_K\boldsymbol{\omega}^i_{KE}\right)\right. \tag{36}$$

$$\left. + \sum_{m=1}^{N^i_U}\frac{\overline{G_iU^m_i}}{L_0}\times\boldsymbol{f}_{U,im} + \sum_{n=1}^{N^i_D}\frac{\overline{G_iD^n_i}}{L_0}\times\boldsymbol{f}_{D,in}\right], \tag{37}$$

with $\boldsymbol{f}^i_A$ and $\boldsymbol{m}^i_A$ the normalized aerodynamic force and torque about the center of mass of aircraft i given in Eqs. (26) and (27). In the above set of equations one also finds $\boldsymbol{f}_{U,im}$ and $\boldsymbol{f}_{D,in}$, which are the normalized elastic forces that tethers linked at the attachment points U^m_i and D^n_i exert on aircraft number i. The explicit form of these forces are given in the next section, where a particle-based model for the tethers is introduced.

B. Equations of motion of the tethers

Let us consider an elastic tether connecting aircraft $i-1$ and i with tips at points D^n_{i-1} and U^m_i. Such a tether has an unstretched length L, diameter D_t, cross-section $A_t = \pi D_t^2/4$, mass $M_t = \rho_t L A_t$, and Young modulus E_t. Our model substitutes each elastic tether by N_P particles

of mass $M_P = M_t/N_P$ and cross-section $A_P = A_t/N_P$ linked by $N_P + 1$ dampers and springs. The latter has natural length $L/(N_P + 1)$ and elastic force proportional to the product $E_t A_t$. The S_E-components for the position and velocity vectors of each of these particles are written as $\boldsymbol{R}_P^k \equiv L_0 \boldsymbol{r}_P^k = L_0 \left(x_P^k \boldsymbol{x}_E + y_P^k \boldsymbol{y}_E + z_P^k \boldsymbol{z}_E \right)$ and $\boldsymbol{V}_P^k \equiv \sqrt{gL_0} \boldsymbol{v}_P^k = \sqrt{gL_0} \left(\dot{x}_P^k \boldsymbol{x}_E + \dot{y}_P^k \boldsymbol{y}_E + \dot{z}_P^k \boldsymbol{z}_E \right)$, $k = 1 \ldots N_P$.

According to the previous notation, the modulus of the elastic force at a particle with index k is

$$F_S^k = E_t A_t \left(\frac{N_P + 1}{L} |\boldsymbol{R}_P^k - \boldsymbol{R}_P^{k-1}| - 1 \right) \tag{38}$$

or, in normalized form

$$f_S^k \equiv \frac{F_S^k}{M_K^1 g} = \frac{E_t A_t}{M_K^1 g} \left(\chi |\boldsymbol{r}_P^k - \boldsymbol{r}_P^{k-1}| - 1 \right) \tag{39}$$

with $\chi \equiv (N_P + 1) L_0 / L$. The equations of motion of the particles then reads

$$\frac{d^2}{d\tau^2} \begin{pmatrix} x_P^k \\ y_P^k \\ z_P^k \end{pmatrix} = \begin{pmatrix} 0 \\ 0 \\ 1 \end{pmatrix} + \frac{1}{\sigma_P} \left(\boldsymbol{f}_{AP}^k + \boldsymbol{f}_T^{k+1} - \boldsymbol{f}_T^k \right) \tag{40}$$

with k running from 1 to N_P. In Eq. (40) we introduced the parameter $\sigma_P = M_P / M_{K1}$ and the normalized aerodynamic drag and tether forces

$$\boldsymbol{f}_{AP}^k = - \frac{\rho A_P C_D}{2 M_K^1 g} v_{AP}^k \boldsymbol{v}_{AP}^k, \tag{41}$$

$$\boldsymbol{f}_T^j = \begin{cases} \frac{E_t A_t}{M_K^1 g} \left(\epsilon_j + \nu \dot{\epsilon}_j \right) \frac{\boldsymbol{r}_P^j - \boldsymbol{r}_P^{j-1}}{|\boldsymbol{r}_P^j - \boldsymbol{r}_P^{j-1}|} & | \quad \epsilon > 0 \\ 0 & \epsilon < 0 \end{cases}, \tag{42}$$

where $\boldsymbol{v}_{AP}^k = \boldsymbol{v}_P^k - \boldsymbol{V}_w / \sqrt{gL_0}$ is the dimensionless aerodynamic velocity of particle with index k. In the final form of the elastic force in Eq. (42) we added a term proportional to a dimensionless

parameter ν that represents the internal dissipation of the tether and the functions

$$\epsilon_j = \chi \mid \boldsymbol{r}_P^j - \boldsymbol{r}_P^{j-1} \mid -1, \tag{43}$$

$$\dot{\epsilon}_j = \chi \frac{\left(\boldsymbol{r}_P^j - \boldsymbol{r}_P^{j-1}\right) \cdot \left(\boldsymbol{v}_P^j - \boldsymbol{v}_P^{j-1}\right)}{\mid \boldsymbol{r}_P^j - \boldsymbol{r}_P^{j-1} \mid}. \tag{44}$$

Since Eq. (42) applies to all the springs, index j runs from 1 to $N_P + 1$.

The dynamics of the aircraft and the chain of springs and masses are coupled. In Eqs. (34) and (37) the forces $\boldsymbol{f}_{U,im}$ and $\boldsymbol{f}_{D,in}$ coincide with the tether forces $-\boldsymbol{f}_T^{N_P}$ and $\boldsymbol{f}_T^1$ obtained after substituting the tethers attached to points U_i^m and D_i^n by the corresponding chains of masses and springs. On the other hand, the tether forces $\boldsymbol{f}_T^{N_P+1}$ and $\boldsymbol{f}_T^1$ appearing in Eq. (40) for $k = N_P$ and $k = 1$ involve $\boldsymbol{r}_P^{N_P+1}$ and $\boldsymbol{v}_P^{N_P+1}$ and $\boldsymbol{r}_P^{-1}$ and $\boldsymbol{v}_P^{-1}$ [see Eqs. (43)-(44)]. Such vectors coincide with the position and velocity vectors of the attachment points U and D. Since the model does not include tether entanglement effects, the results of the simulations are only valid if there is no contact point between tethers. Such feature can be checked after integrating the equations of motion.

IV. Natural modes and open-loop controller of a train of aircraft

The two simulators can be used to study the dynamics of a train of aircraft as far as they are rigid enough to satisfy the assumption of the model. Here we will apply them to a train of aircraft with the physical parameters of Table 1, which are similar to the ones used in Ref. [20] to study the dynamics of a two-line kite. The analysis is restricted to a configuration of identical aircraft linked by tethers of equal properties. The S_K^i-coordinates of the attachment points are also the same for all the aircraft.

A. Results for rigid tethers

One of the most relevant analyses for the application of a train of aircraft to airborne wind energy is the analysis of the symmetric equilibrium state of the train. If the train is used to lift wind turbines to high altitudes, where winds are stronger and steadier, the features of the equilibrium state and its stability become a cornerstone. Such analysis is carried out by introducing the state

	Symbol	Value	Symbol	Value
Environment	g	9.81 m/s^2	ρ	1.225 kg/m^3
	H_0	27.5 m	H_r	2.1 m
	V_{w0}	4.4 m/s		
Tether	L	100 m	D_{t}	2 mm
	ρ_{t}	970 kg/m^3	C_{D}	1
	E_{t}	90 GPa	ν_{t}	0.01
Aircraft	M_{K}	4 kg	S_{K}	14.4 m^2
	b_{K}	5.8 m	c_{K}	1.5 m
	I_{xx}	21.1 kgm^2	I_{yy}	4.7 kgm^2
	I_{zz}	17.9 kgm^2	I_{xz}	0. kgm^2
	C_{x0}	-0.065	$C_{\mathrm{x}\alpha}$	0.18
	$C_{\mathrm{y}\beta}$	-1.6	C_{z0}	0.12
	$C_{\mathrm{z}\alpha}$	-3.0	$C_{\mathrm{l}\beta}$	0.1
	C_{lp}	-0.15	$C_{\mathrm{n}\beta}$	-0.03
	C_{nr}	-0.002	C_{m0}	0.13
	$C_{\mathrm{m}\alpha}$	-0.76	C_{mq}	-0.17
	$C_{\mathrm{l}\delta_{\mathrm{a}}}$	0	$C_{\mathrm{n}\delta_{\mathrm{r}}}$	0
	$C_{\mathrm{m}\delta_{\mathrm{e}}}$	-1.54	V_{T}	7 m/s
Attachment	X_{U}	0.75 m	X_{D}	0
Points	Y_{U}	2.9 m	Y_{D}	0
	Z_{U}	2.0 m	Z_{D}	0

Table 1 Parameters of the system. The moments of inertia were normalized as $\iota_{ij} = I_{ij}/M_K^1 L_0^2$ $(i,j = x,y)$ and the attachment point coordinates $x_i = X_i/L_0$, $y_i = Y_i/L_0$, and $z_i = Z_i/L_0$ $(i = U,D)$.

vector $\boldsymbol{x}_s = [\boldsymbol{q}_s \quad \dot{\boldsymbol{q}}_s]$ and the control vector $\boldsymbol{x}_c(\tau) = [\delta_a^1 \ \delta_r^1 \ \delta_e^1 \ \ldots \delta_a^{N_K} \ \delta_r^{N_K} \ \delta_e^{N_K}]$, and writing equations (29) as

$$\frac{d\boldsymbol{x}_s}{d\tau} = \boldsymbol{f}\left(\boldsymbol{x}_s; \boldsymbol{x}_c\right). \tag{45}$$

Without control, i.e. setting $\delta_a^i = \delta_r^i = \delta_e^i = 0$ for $i = 1 \ldots N_K$, the equilibrium states $\boldsymbol{x}_s^*$ are found by solving the nonlinear set of algebraic equations $\boldsymbol{f}(\boldsymbol{x}_s^*) = 0$ with Newton's method. One half of the variables are obviously known ($\dot{\boldsymbol{q}}_s = 0$) and the analysis is also restricted to symmetric equilibrium states that have $\varphi_i = 0$ and $\eta_i = 0$. Therefore, there are only $2N_K$ unknowns in the system $\boldsymbol{f}(\boldsymbol{x}_s^*) = 0$. Once $\boldsymbol{x}_s^*$ is known, we can recover all the interesting physical quantities such as the positions of the aircraft, the tether tensions, angles of attack, etc.

Figure 2 displays some interesting information about two different trains with $N_K = 10$ and $N_K = 20$ and the parameters of Table 1. Panel (a), which shows the position of the centers of mass

of the aircraft, reveals that the elevation angle of the train is practically independent on the number of aircraft for this model, which ignores tether mass and aerodynamic drag. Moreover, according to panel (b), the angles of attack of the aircraft are practically constant with the position of the aircraft within the train. Such enhancement is a little more pronounced for the uppermost aircraft. On the other hand, the modulus of the tension at the attachment point U^+, which coincides with the one at U^- because the equilibrium state is symmetric, is maximum at the aircraft closest to the ground and it decreases with the aircraft position. The tethers linked to the uppermost aircraft are subjected to the lowest mechanical loads.

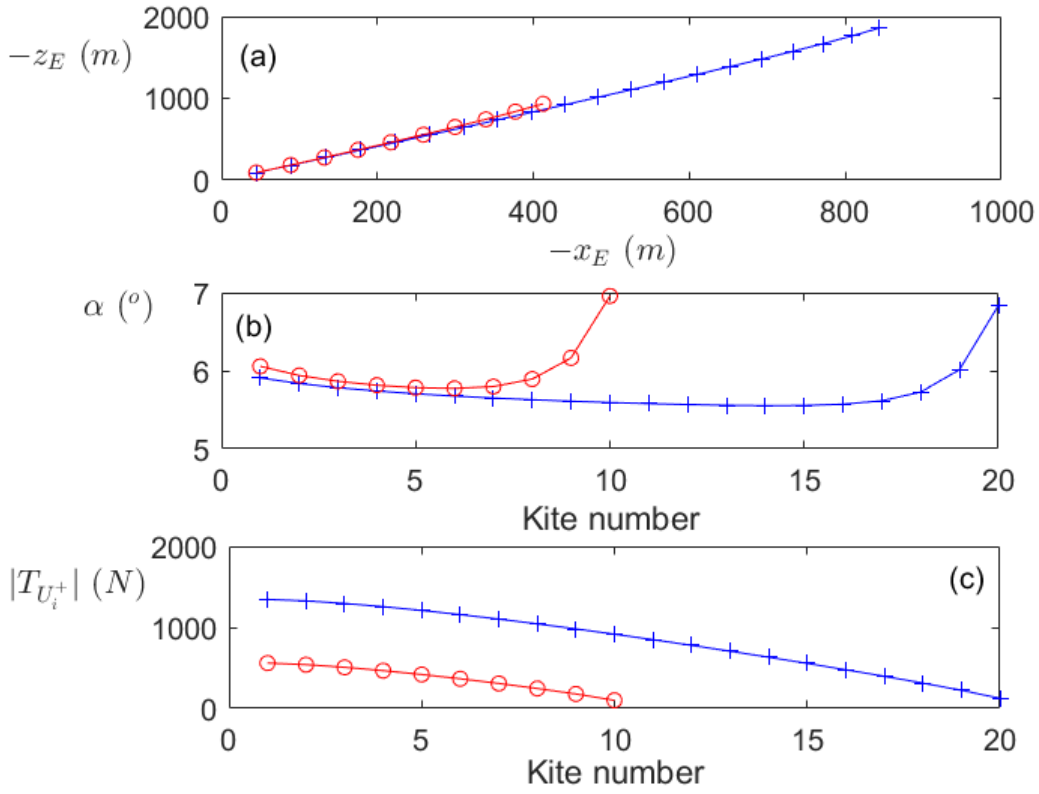

Fig. 2 Position (top), and angle of attack (middle) and tether tension (bottom) versus aircraft number for two trains of aircraft linked by inelastic tethers.

The linear stability of $\boldsymbol{x}_s^*$ is studied by adding a small perturbation $\boldsymbol{x}_{1s}$ to the equilibrium state and substituting $\boldsymbol{x} = \boldsymbol{x}_s^* + \boldsymbol{x}_{1s}$ in Eq. (45). After doing a Taylor expansion and dropping second order terms, it becomes $d\boldsymbol{x}_{1s}/d\tau = \boldsymbol{J}\,|_{\boldsymbol{x}_s^*}\,\boldsymbol{x}_{1s}$, with $\boldsymbol{J}\,|_{\boldsymbol{x}_s^*}$ the Jacobian matrix of the flow $\boldsymbol{f}$ evaluated at the equilibrium state. The stability of $\boldsymbol{x}_s^*$ is governed by the eigenvalues λ_j of $\boldsymbol{J}\,|_{\boldsymbol{x}_s^*}$. Each eigenvalue corresponds to a natural mode and it is asymptotically stable if the real part of λ_j

is negative. In the linear approximation, the motion of the train associated with each eigenvalue j is governed by the eigenvector $\tilde{\boldsymbol{e}}_j$ of $\boldsymbol{J}\,|_{\boldsymbol{x}_s^*}$ (natural mode).

Thanks to the choice of coordinates and the aerodynamic model implemented, the jacobian matrix $\boldsymbol{J}\,|_{\boldsymbol{x}_s^*}$ has a block-like structure and the longitudinal and lateral-directional modes are decoupled. The former involve the coordinates γ_i and θ_i and the latter φ_i and η_i. The jacobian matrix was computed with a finite difference scheme and its block-structure was then used to find the two submatrices describing the longitudinal and lateral-directional modes. Tables 2 and 3 show the eigenvalues and eigenvectors of the longitudinal and lateral-directional modes of an aircraft with the parameters of Table 1. The interpretation of these results is straightforward. For instance, since its eigenvector components associated to γ_1 and $\dot{\gamma}_1$ are very small, the third longitudinal mode corresponds to a highly damped oscillatory pitch motion of the aircraft that keeps the elevation angle of the tethers almost constant. Note that, according to the definition given in Sec. II, θ is not the pitch angle but it is directly related to it.

Mode	1	2	3
Eigenvalue	-0.71	-4.4	$-16.6 \pm 36.8i$
Eigenvector			
γ_1	1	-0.03	$0.00017 \pm 0.00038i$
θ_1	0.29	-0.22	$-0.010 \pm 0.022i$
$\dot{\gamma}_1$	-0.71	0.14	$-0.017 \pm 0.00008i$
$\dot{\theta}_1$	-0.21	1	1.0

Table 2 Longitudinal modes for $N_K = 1$ and rigid tethers.

Mode	1	2	3
Eigenvalue	-0.019	$-1.03 \pm 0.50i$	-72.8
Eigenvector			
φ_1	0.26	$-0.78 \pm 0.38i$	-0.0023
η_1	1	$-0.23 \pm 0.04i$	-0.014
$\dot{\varphi}_1$	-0.005	1	0.17
$\dot{\eta}_1$	-0.02	$0.26 \pm 0.075i$	1

Table 3 Lateral modes for $N_K = 1$ and rigid tethers

Table 4 shows the eigenvalues of the longitudinal and lateral-directional modes of a train of two aircraft. The real parts of all the eigenvalues are negative and the equilibrium state is stable. A comparative analysis of the eigenvalues with the case $N_K = 1$ reveals some interesting features.

For instance, for $N_K = 1$, there is a natural mode with eigenvalue $-16.6 \pm 36.8i$, whose eigenvector is dominated by $\dot{\theta}_1$. For $N_K = 2$ there are two similar modes with eigenvalues $-13.4 \pm 40.5i$ and $-24.8 \pm 43.7i$ and for both of them the corresponding eigenvectors are dominated by the two components $\dot{\theta}_1$ and $\dot{\theta}_2$. Although we do not provide here the values of the eigenvectors, interested readers can readily get them by using the open-source code. A similar behavior happens for the lateral-directional mode with -72.8 for $N_K = 1$ and -72.6 and -86.2 for $N_K = 2$. Increasing the number of aircraft also generates new modes; an example is the complex eigenvalue $-3.2 \pm 0.71i$ for $N_K = 2$.

Aircraft Longitudinal	Aircraft Lateral
-0.44	-0.017
$-3.2 \pm 0.71i$	-0.036
-6.48	-0.92
$-13.4 \pm 40.5i$	$-1.27 \pm 0.73i$
$-24.8 \pm 43.7i$	-1.52
	-72.6
	-86.2

Table 4 Eigenvalues of the natural modes of a train of aircraft with $N_K = 2$ and rigid tethers.

However, the main application of KiteTrain is not the modal analysis of a single aircraft or a two-aircraft train but the understanding of the collective modes of a train with a large number of aircraft. In particular, we are interested in the identification of the coordinates of the state vector that are more easily excited when the train of aircraft is perturbed from its equilibrium state. For instance, in the case of the longitudinal modes, there are $4N_K$ eigenvectors that we denote as $\tilde{\boldsymbol{e}}_j$, $j = 1 \dots 4N_K$. From them we can construct another vector $\boldsymbol{\kappa}_L$ with components

$$\kappa_L^i = \sum_{j=1}^{4N_K} \Big(|\tilde{e}_j^{2(i-1)+1}| + |\tilde{e}_j^{2i}| + |\tilde{e}_j^{2(N_K+i-1)+1}| + |\tilde{e}_j^{2(N_K+i)}| \Big) \tag{46}$$

where $i = 1 \dots N_K$ and $\tilde{e}_j^k$ is the k-th component of the longitudinal eigenvector $\tilde{\boldsymbol{e}}_j$. According to Eq. (46), κ_L^i picks up the contribution of the longitudinal coordinates of aircraft i, which are γ_i, θ_i, $\dot{\gamma}_i$ and $\dot{\theta}_i$, to all the longitudinal modes. Therefore, the component κ_L^i gives information of the level

of participation of aircraft i to all the longitudinal modes of the train. A similar vector $\boldsymbol{\kappa}_D$ can be defined for the lateral-directional modes.

Panel (a) in Fig. 3 shows κ_L^i normalized over its own modulus $|\boldsymbol{\kappa}_L|$ versus the aircraft number i for $N_K = 20$. Since κ_L^i grows monotonically with the aircraft index, we conclude that, in average, the coordinates of certain aircraft are more easily excited in the longitudinal modes if such an aircraft has a higher position within the train. According to this result, the coordinates of the uppermost aircraft, i.e. γ_{N_K}, θ_{N_K}, $\dot{\gamma}_{N_K}$, $\dot{\theta}_{N_K}$, are the most prone to be excited in the longitudinal modes. As shown in panel (b), a similar behavior is observed for the lateral modes. These conclusions are only valid in the linear approximation, i.e. small displacements, and a nonlinear analysis is needed to study the motion of the train of aircraft faraway from the symmetric equilibrium configuration. The effect of the wind velocity profile was studied by repeating this analysis for a constant wind velocity equal to $V_w = 7$ m/s (instead of the wind shear profile of Eq. (1)). The study (not shown), reveals that the behaviors of κ_L^i versus the aircraft number for shear and constant wind profiles are similar. However, the distribution of κ_D^i with the aircraft number is flatter, reaches a soft maximum around $2N_K/3$, and exhibits a singular peak at the uppermost aircraft ($i = N_K$) for the constant wind profile. Therefore, it is concluded that, independently of the wind velocity profile, the longitudinal and lateral coordinates of the uppermost aircraft are the most prone to be excited.

Besides analysis of the modes (linear theory), the simulator can be used to explore the nonlinear dynamics of trains of aircraft. In order to illustrate this capability, and also the implementation of open-loop controllers, we considered the longitudinal dynamic of a train of 5 aircraft with the properties of Table 1. All the control variables are zero except the deflections of the elevators, which follow the temporal law

$$\delta_e^i(t) = \delta_0 \cos(\omega_{\delta_e} \tau), \qquad i = 1 \ldots 5 \tag{47}$$

with $\delta_0 = 3^\circ \times \pi/180 = 0.052$ rad and $\omega_{\delta_e} = 0.05 rad/s \times \sqrt{L_0/g} = 0.16$. If Eqs. (45) are integrated with initial condition equal to the equilibrium state found without control but the control law given by Eq. (47), the system naturally converges to a stable periodic orbit. As shown in panel (a) of Fig.

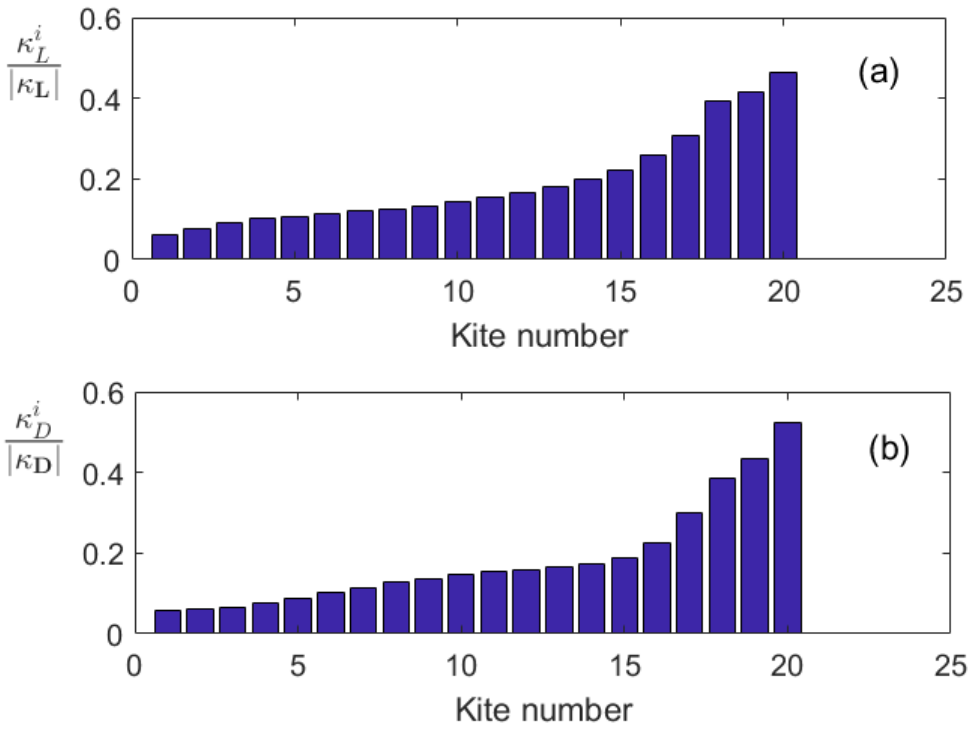

Fig. 3 Panels (a) and (b) show the indices κ_L and κ_D versus the aircraft number for $N_K = 20$.

4, the train performs oscillations with period $\tau_0 = 2\pi/\omega_{\delta_e}$, which is around 125.7 s. Panel (b) and (c) display the evolution of the angles of attack and the modulus of the tether tensions at points U_i^+ and U_i^-, which are equal because the maneuver is symmetric. For convenience, these variables for the uppermost and lowermost aircraft were plotted with thick and dashed lines, respectively. The highest angle of attack is reached by the uppermost aircraft, which is the least constrained body (see panel (b)). The highest tension is reached at the lowermost aircraft, which also supports the largest amplitude variations of the force.

B. Results for elastic tethers

Previous results in Sec. IV A ignored elasticity (infinite Young modulus), flexibility, inertia (mass) and aerodynamic drag effects on the tethers. We now investigate one by one the impact of all these effects in the dynamics by using KiteElastic module. As a preliminary step, the correct implementation of the codes was verified by comparing the equilibrium state and the natural modes given by both modules for a similar train of aircraft. With this aim, KiteElastic was configured

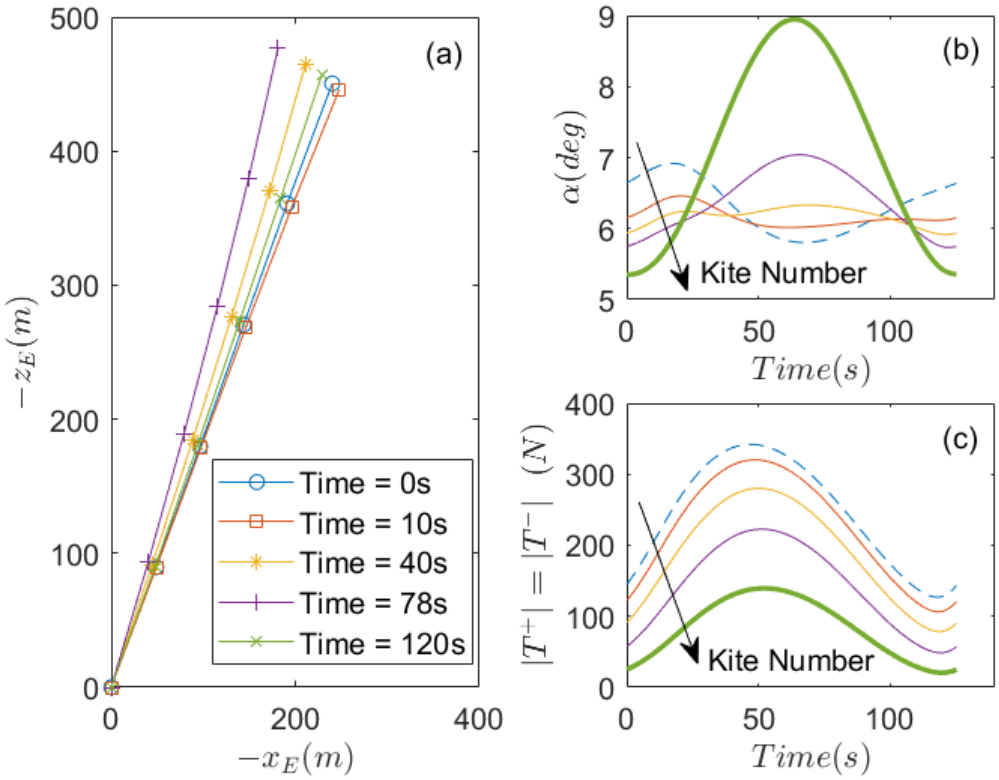

Fig. 4 Periodic orbit of a train of 5 aircraft with an open-loop controller.

with $N_K = 1$, $N_P = 1$. We also took a finite Young modulus of $E_t = 90$GPa and tether diameter $D_t = 2$mm, but ignored the tether aerodynamic drag ($C_D = 0$) and internal friction ($\nu_t = 0$). We also set an unrealistic tether density of $\rho_t = 100\text{kg/m}^3$ to reduce inertial effects and compare both codes. It was found that the equilibrium states, i.e. the position of the center of mass of the aircraft and its angle of attack, given by both codes match perfectly.

The comparison of the natural modes, which enclose information about the stability of the equilibrium state, is a bit more delicate because, for this particular configuration, the state vectors of KiteTrain and KiteElastic have dimensions equal to 8 and 24, respectively. The number of modes in the elastic model is obviously larger because the aircraft has no constraint, i.e. 12 components in the state vector, and each tether introduces 6 components more in the state vector (position and velocity of each mass). Table 5 shows the eigenvalues of the Jacobian matrix for KiteElastic evaluated at the equilibrium state. Although all eigenvectors mix aircraft and tether coordinates, a detailed inspection reveals that there are dominant components. For this reason, we classified the natural modes as *aircraft* and *tether* modes. Moreover, the dominant component of the eigenvector

in the *aircraft* modes allows them to be classified as longitudinal and lateral modes. Regarding tether modes, the magnitude of the angular frequency of the mode (imaginary part of the eigenvalue) separates the tether modes into fast (mainly longitudinal oscillations) and slow (lateral oscillations).

An inspection of Tables 2, 3, and Table 5 reveals that all the longitudinal and lateral-directional modes of the system in the simplified model, i.e. with straight inelastic tethers without inertia, are a subset of the more complex model. This is also evident from Fig. 5, which shows the eigenvalues in the complex plane for the two models. The two insets display particular regions of the diagram. Figure 5 shows that there is only a significant difference for the damping (real part) of a longitudinal mode characterized by a complex eigenvalue. It was checked that this difference disappears when the Young modulus of the elastic tethers is increased. For instance, moving from $E_t = 90GPa$ to $E_t = 200GPa$ changes the eigenvalue from $\lambda = -11.6 \pm 41.9i$ to $\lambda = -15.23 \pm 39.32i$, which is closer to the eigenvalue provided by the model with inelastic tethers ($\lambda = -16.6 \pm 36.8i$). Such agreement is a means to cross-check the correct implementation of the codes.

It is also interesting that a finite value of the Young modulus, i.e. removing the geometrical constraints used in Sec. II (constant tether lengths), adds extra longitudinal and lateral aircraft modes. According to the values of the real parts of the corresponding eigenvalues, these two modes are highly damped. Regarding the tethers, the appearance of fast modes in the elastic model is detrimental for the performance of the simulator. The imaginary part of the eigenvalues of the fast tether modes are between one and two orders of magnitude higher than the slow tether modes and the aircraft modes. Therefore, the system presents two separate time scales and the numerical integration should be done carefully (stiff problem). Such a fast scale has a period of $\sim 2\pi/1920\sqrt{L_0/g} \approx 0.01$s and it corresponds to longitudinal oscillations with velocity $\sim \sqrt{E_t/\rho_t} = 30000m/s$. Both numbers are in agreement because the time needed by a longitudinal perturbation to travel a round trip throughout the tether at such a velocity is about $2L_0/30000\text{m/s} \approx 0.007$s. Regarding the slow tether modes, the most relevant feature is that one of them has a positive real part, thus changing the stability character of the equilibrium state. For this particular set of parameters, the it is unstable.

Table 6 shows the eigenvalues of the natural modes for the same parameters of Table 5 but $N_K =$

Aircraft Longitudinal	Aircraft Lateral	Tether Fast	Tether Slow
-0.72	-0.012	$-0.06 \pm 1922i$	$+0.004 \pm 22.1i$
-4.3	$-1.0 \pm 0.48i$	$-0.24 \pm 1919i$	$-0.0002 \pm 21.9i$
$-11.6 \pm 41.9i$	$-9.3 \pm 155.0i$		$-0.014 \pm 21.9i$
$-64.6 \pm 94.2i$	-72.8		$-0.082 \pm 23.8i$

Table 5 Eigenmodes with $N_K = 1$, $N_P = 1$, no tether drag and friction, and small tether inertia.

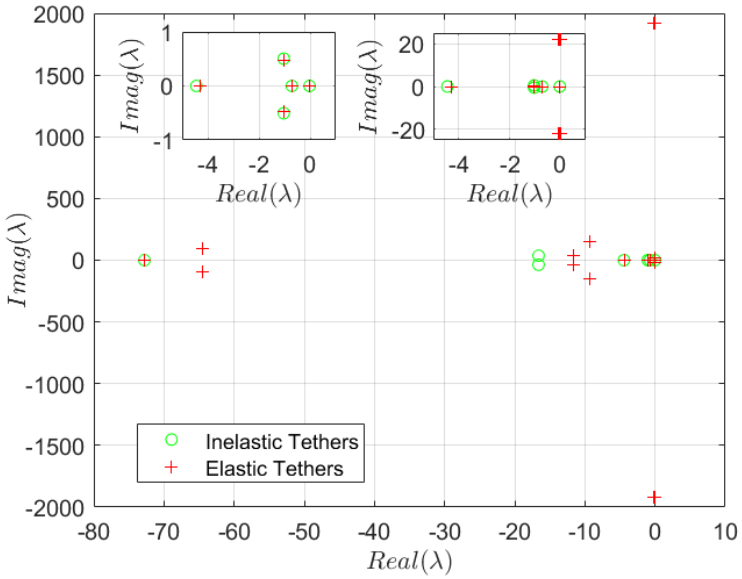

Fig. 5 Eigenvalues of the natural modes from Tables 2 and 3 (inelastic tethers) and Table 5 (elastic tethers with Young modulus equal to 90GPa). $N_K = 1$

2. A comparison, with Table 4 and also Fig. 6, show again that the natural modes (longitudinal and lateral-directional) obtained with KiteTrain are a subset of the modes obtained with KiteElastic. The main difference between both models happens for the damping (real part) of two couples of complex conjugated eigenmodes. There is a slow mode that is weakly unstable.

In order to evaluate tether inertial and drag effects in the dynamics of a train of aircraft, we set the parameters of Table 1 and $N_P = 3$, $E_t = 90$GPa, $D_t = 2$mm, $C_D = 1$, $\nu_t = 0.01$, and $\rho_t = 970\text{kg/m}^3$. Following Sec. IV A, we did the analysis for $N_K = 10$ and $N_K = 20$ and, although the main results are very similar, there are some interesting differences. In both cases the angles of attack of the aircraft are almost independent on the position of the aircraft. However, as shown in panel (b) of Fig. 7, the angle α_i now slightly decreases with i. The tether tension at point U_i^1, which is the same as in U_i^2 because the state is symmetric, is higher than in Sec. IV A. Both differences

Aircraft Longitudinal	Aircraft Lateral	Tether Fast	Tether Slow
$-0.21 \pm 32.4i$	-0.0016	$-0.062 \pm 1922i$	$+0.0017 \pm 26.3i$
-0.45	-0.003	$-0.088 \pm 1922i$	$-0.00013 \pm 32.5i$
$-3.1 \pm 0.68i$	-0.91	$-0.1 \pm 1917i$	$-0.00024 \pm 26.2i$
$-3.5 \pm 43.6i$	$-1.2 \pm 0.7i$	$-0.67 \pm 1925i$	$-0.0018 \pm 32.6i$
-6.0	-1.5		$-0.032 \pm 26.25i$
$-12.18 \pm 43.8i$	$-9.1 \pm 155.4i$		$-0.024 \pm 32.5i$
$-65.9 \pm 178.1i$	$-13.2 \pm 154.4i$		$-0.08 \pm 26.2i$
$-84.5 \pm 18.4i$	-72.6		
	-86.3		

Table 6 Eigenmodes with $N_K = 2$, $N_P = 1$, no tether drag and friction, and small tether inertia.

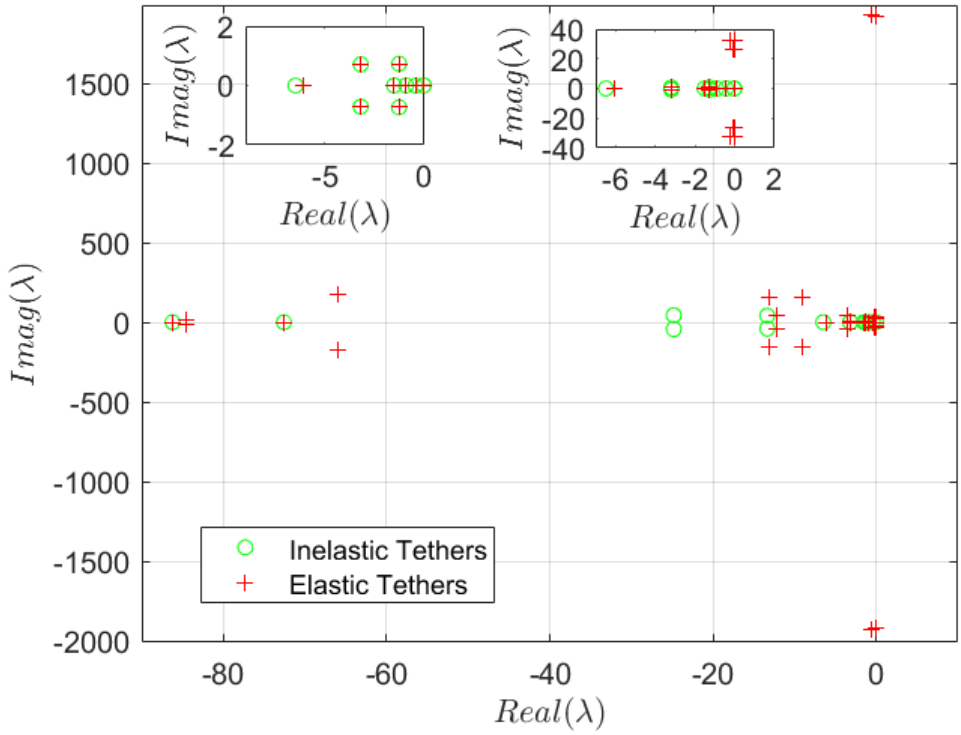

Fig. 6 Eigenvalues of the natural modes from Table 4 (inelastic tethers) and Table 6 (elastic tethers with Young modulus equal to 90GPa). $N_K = 2$.

are consequences of the aerodynamic drag on the tether (the results of Sec. IV A are recovered by setting $C_D = 0$).

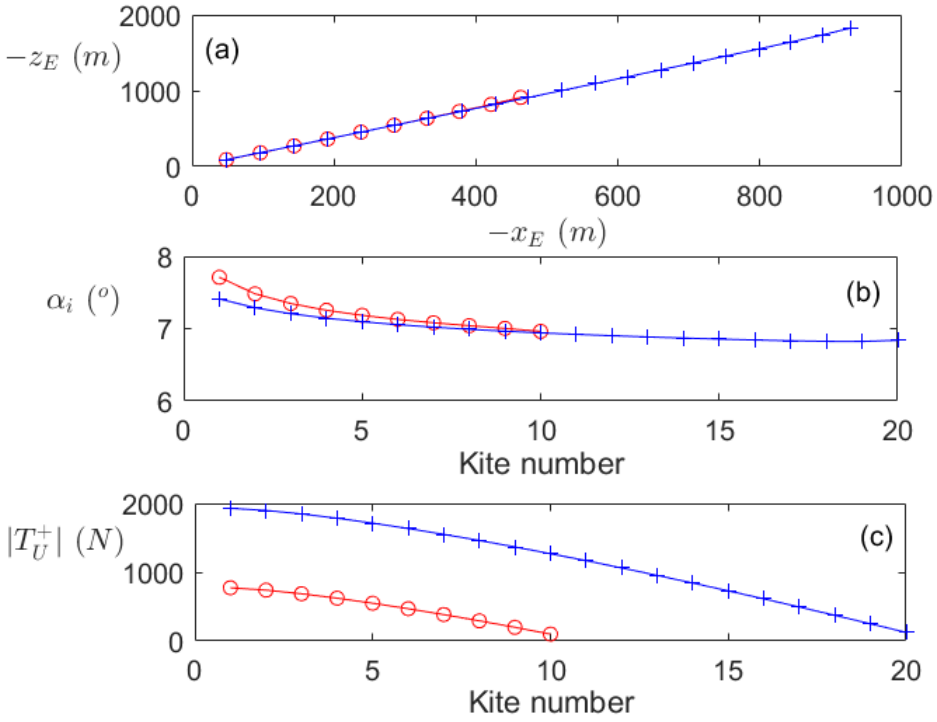

Fig. 7 Equilibrium of two trains of aircraft. Tether mass, aerodynamic drag, and elasticity effects are included.

V. Conclusions

The work presented two flight simulators to investigate the dynamics and stability of different types of AWE systems based on multi-aircraft configurations. The first simulator (KiteTrain) has been designed to study a very particular configuration: a train of stacked aircraft made of an arbitrary number of aircraft and linked among them by two tethers. Its most important drawbacks are the very simplistic model for the tethers (tether inertia, elasticity, and aerodynamic drag are ignored) and the lack of flexibility of its architecture. Any change in the model, like for instance adding a third tether to connect the aircraft, would require one to rebuild the simulator. However, the actual code is very efficient because a pure set of non-stiff ordinary differential equations has been obtained by using a Lagrangian formulation with a minimum coordinate approach. These advantages and limitations suggest that this code may have two main applications: (i) the analysis of the dynamics and stability of trains made of a very large number of aircraft, and (ii) cross-checking and verifying the correct implementation of other multi-aircraft simulators with a more flexible architecture. Regarding the first, this work carried out a preliminary analysis of the symmetric

equilibrium state of the train and performed a modal analysis varying the number of aircraft in the train. Tether tensions and angle of attack distribution along the train have been obtained. The analysis of the modes showed that, the higher the position of the aircraft in the train, the more they participate in the longitudinal and the lateral modes.

The characteristics of the second simulator (KiteElastic) are complementary to the ones of the KiteTrain and its objectives, applications, and scope, are different. First, the model of the tethers is much more detailed because it includes tether inertial, elasticity, and aerodynamic drag effects. Second, the architecture of the code is flexible because it simulates an arbitrary number of rigid aircraft linked among them by an arbitrary number of tethers. The mechanical system is configured by the user according to the particular needs. However, since the tethers are elastic and the Young modulus is typically very large, the equations of motions are stiff because they incorporate the fast longitudinal waves of the tethers. Consequently, for equal number aircraft, the computational cost of KiteElastic is much larger than the one for KiteTrain.

The comparative analysis of the equilibrium state and the natural modes allowed us a cross-verification of the implementation of both codes. It also highlighted some interesting consequences induced by the elastic character of the tethers and their aerodynamic drag. First, as already mentioned, tether elasticity introduces high-frequency modes. Second, inertial effects (finite mass and weight) and aerodynamic drag on the tethers increase the values of the equilibrium angles of attack of the aircraft and the tether tensions.

Since aircraft fly in cross wind conditions along a planned path in most of airborne wind energy applications, the incorporation of control variables in the simulators is essential. In this work, the control was added in the aerodynamic torque through the deflections of control surfaces like elevators, ailerons, and rudders. This capability, which belongs to both codes, was shown by simulating a simple longitudinal maneuver with an open-loop controller. Alternative control means, like tether length modulation, requires a higher analytical effort and the revision of the equations of motion of the simulators. The codes can be readily combined with nonlinear optimization solvers and used to investigate the efficiency of airborne wind energy machines based on multi-aircraft configurations. Nevertheless, the simulation of highly nonlinear maneuvers necessarily demands a better aerody-

namic model than the one used in this work, which is only valid within a limited range of attack and sideslip angles.

Acknowledgments

This work was supported by the Ministerio de Ciencia, Innovación y Universidades of Spain and the European Regional Development Fund under the GreenKite project ENE2015-69937-R (MINECO/FEDER, UE) and continued under the GreenKite-2 project funded by Agencia Estatal de Investigación (PID2019-110146RB-I00/ AEI / 10.13039/501100011033). GSA work is supported by the Ministerio de Ciencia, Innovación y Universidades of Spain under the Grant RYC-2014-15357.

APPENDIX A: AUXILIARY CALCULATIONS

Using in Eq. (13) the rotation matrices given in Eqs. (7), (8), and (9) yields the S_E-component of the position vector of aircraft i

$$\begin{aligned}\boldsymbol{r}_i =& \boldsymbol{r}_{i-1} + \\ & - \left[\left(x_U^i c\theta_i + z_U^i s\theta_i\right) c\gamma_i c\varphi_i + \left(\xi_i - x_U^i s\theta_i + z_U^i c\theta_i\right) \cdot \right. \\ & \cdot \left(c\eta_i s\gamma_i c\varphi_i + s\eta_i s\varphi_i\right) + \zeta_i \left(s\eta_i s\gamma_i c\varphi_i - c\eta_i s\varphi_i\right)\Big] \boldsymbol{x}_E \\ & - \left[\left(x_U^i c\theta_i + z_U^i s\theta_i\right) c\gamma_i s\varphi_i + \left(\xi_i - x_U^i s\theta_i + z_U^i c\theta_i\right) \cdot \right. \\ & \cdot \left(c\eta_i s\gamma_i s\varphi_i - s\eta_i c\varphi_i\right) + \zeta_i \left(s\eta_i s\gamma_i s\varphi_i + c\eta_i c\varphi_i\right)\Big] \boldsymbol{y}_E \\ & + \left[\left(x_U^i c\theta_i + z_U^i s\theta_i\right) s\gamma_i - \left(\xi_i - x_U^i s\theta_i + z_U^i c\theta_i\right) \cdot \right. \\ & \cdot c\eta_i c\gamma_i - \zeta_i s\eta_i c\gamma_i\Big] \boldsymbol{z}_E \end{aligned} \tag{A1}$$

Taking the τ-derivative of Eq. (A1) one finds Eq. (20). The tensor $\bar{\boldsymbol{\Xi}}(\varphi, \gamma, \eta, \theta, d, x_A, z_A)$ is

given by

$$\begin{aligned}
\Xi_{11} =&(x_U c\theta + z_U s\theta)c\gamma s\varphi + (\xi - x_U s\theta + z_U c\theta)\cdot \\
&\cdot (c\eta s\gamma s\varphi - s\eta c\varphi) + \zeta\,(c\eta c\varphi + s\eta s\gamma s\varphi) && \text{(A2)} \\
\Xi_{12} =&(x_U c\theta + z_U s\theta s\gamma c\varphi) - (\xi - x_U s\theta + z_U c\theta)c\eta c\gamma c\varphi \\
&- \zeta s\eta c\gamma c\varphi && \text{(A3)} \\
\Xi_{13} =&(\xi - x_U s\theta + z_U c\theta)(s\eta s\gamma c\varphi - c\eta s\varphi) \\
&- \zeta\,(s\eta s\varphi + c\eta s\gamma c\varphi) && \text{(A4)} \\
\Xi_{14} =&(x_U s\theta - z_U c\theta)c\gamma c\varphi + (x_U c\theta + z_U s\theta)(c\eta s\gamma c\varphi + s\eta s\varphi) && \text{(A5)} \\
\Xi_{21} =&-(x_U c\theta + z_U s\theta)c\gamma c\varphi - (\xi - x_U s\theta + z_U c\theta)\cdot \\
&\cdot (c\eta s\gamma c\varphi + s\eta s\varphi) + \zeta\,(c\eta s\varphi - s\eta s\gamma c\varphi) && \text{(A6)} \\
\Xi_{22} =&(x_U c\theta + z_U s\theta)s\gamma s\varphi - (\xi - x_U s\theta + z_U c\theta)c\eta c\gamma s\varphi \\
&- \zeta s\eta c\gamma s\varphi && \text{(A7)} \\
\Xi_{23} =&(\xi - x_U s\theta + z_U c\theta)(s\eta s\gamma s\varphi + c\eta c\varphi) \\
&+ \zeta\,(s\eta c\varphi - c\eta s\gamma s\varphi) && \text{(A8)} \\
\Xi_{24} =&(x_U s\theta - z_U c\theta)c\gamma s\varphi + (x_U c\theta + z_U s\theta)(c\eta s\gamma s\varphi - s\eta c\varphi) && \text{(A9)} \\
\Xi_{31} =&0 && \text{(A10)} \\
\Xi_{32} =&(x_U c\theta + z_U s\theta)c\gamma + (\xi - x_U s\theta + z_U c\theta)c\eta s\gamma + \zeta s\eta s\gamma && \text{(A11)} \\
\Xi_{33} =&(\xi - x_U s\theta + z_U c\theta)s\eta c\gamma - \zeta c\eta c\gamma && \text{(A12)} \\
\Xi_{34} =&-(x_U s\theta - z_U c\theta)s\gamma + (x_U c\theta + z_U s\theta)c\eta c\gamma && \text{(A13)}
\end{aligned}$$

and $\bar{\boldsymbol{X}}\left(\varphi,\gamma,\eta,\xi,\eta\right)$ is

$$\begin{aligned}\bar{\boldsymbol{X}} = &-\begin{pmatrix} c\eta s\gamma c\varphi + s\eta s\varphi \\ c\eta s\gamma s\varphi - s\eta c\varphi \\ c\eta c\gamma \end{pmatrix}\nabla_{\boldsymbol{q}_s}\xi \\ &-\begin{pmatrix} s\eta s\gamma c\varphi - c\eta s\varphi \\ s\eta s\gamma s\varphi + c\eta c\varphi \\ s\eta c\gamma \end{pmatrix}\nabla_{\boldsymbol{q}_s}\eta \end{aligned} \tag{A14}$$

The terms $\nabla_{\boldsymbol{q}_s}\xi$ and $\nabla_{\boldsymbol{q}_s}\zeta$ in Eq. (A14) are found by taking the gradient operator

$$\nabla_{\boldsymbol{q}_s} = \begin{bmatrix} \dfrac{\partial}{\partial\varphi_1} & \dfrac{\partial}{\partial\gamma_1} & \dfrac{\partial}{\partial\eta_1} & \dfrac{\partial}{\partial\theta_1}\cdots & \dfrac{\partial}{\partial\eta_{N_k}} & \dfrac{\partial}{\partial\theta_{N_k}} \end{bmatrix} \tag{A15}$$

in Eq. (17). Such operation involves the gradients of $C_{xi}^{\pm}$, $C_{yi}^{\pm}$, and $C_{zi}^{\pm}$, which are computed easily by noting that the only terms involving $\boldsymbol{q}_s$ in Eq. (15) are included in the matrix

$$\begin{aligned}\bar{\boldsymbol{R}}_{2E}^{i}\bar{\boldsymbol{R}}_{EK}^{i-1} = &\bar{\boldsymbol{R}}_{21}^{i}\left(\eta_i\right)\bar{\boldsymbol{R}}_{1E}^{i}\left(\varphi_i,\gamma_i\right)\left[\bar{\boldsymbol{R}}_{K2}^{i-1}\left(\theta_{i-1}\right)\right. \\ &\left.\bar{\boldsymbol{R}}_{21}^{i-1}\left(\eta_{i-1}\right)\bar{\boldsymbol{R}}_{1E}^{i-1}\left(\varphi_{i-1},\gamma_{i-1}\right)\right]^{T}\end{aligned} \tag{A16}$$

Therefore, the only non-zero elements of the gradients of $C_{xi}^{\pm}$, $C_{yi}^{\pm}$, and $C_{zi}^{\pm}$ are the ones involving the derivatives with respect to η_i, φ_i, γ_i, φ_{i-1}, γ_{i-1}, η_{i-1}, and θ_{i-1}. One example is

$$\frac{\partial}{\partial\eta_i}\begin{pmatrix} C_{xi}^{\pm} \\ C_{yi}^{\pm} \\ C_{zi}^{\pm} \end{pmatrix} = -\frac{\partial\bar{\boldsymbol{R}}_{21}^{i}}{\partial\eta_i}\bar{\boldsymbol{R}}_{1E}^{i}\bar{\boldsymbol{R}}_{EK}^{i-1}\begin{pmatrix} x_D^{i-1} \\ \pm y_D^{i-1} \\ z_D^{i-1} \end{pmatrix} \tag{A17}$$

REFERENCES

[1] Cristina L. Archer and Mark Z. Jacobson. Evaluation of global wind power. *Journal of Geophysical Research: Atmospheres*, 110(D12), 2005. doi: https://doi.org/10.1029/2004JD005462.

[2] Philip Bechtle, Mark Schelbergen, Roland Schmehl, Udo Zillmann, and Simon Watson. Airborne wind energy resource analysis. *Renewable Energy*, 141:1103 – 1116, 2019. ISSN 0960-1481. doi:

https://doi.org/10.1016/j.renene.2019.03.118.

[3] James Casey and Oliver M. O,Reilly. Geometrical derivation of lagrange,s equations for a system of rigid bodies. *Mathematics and Mechanics of Solids*, 11(4):401–422, 2006. doi: https://doi.org/10.1177/1081286505044137.

[4] J. De Schutter, R. Leuthold, T. Bronnenmeyer, R. Paelinck, and M. Diehl. Optimal control of stacked multi-kite systems for utility-scale airborne wind energy. In *2019 IEEE 58th Conference on Decision and Control (CDC)*, pages 4865–4870, 11-13 December 2019, Nice, France, 12 2019. doi: https://doi.org/10.1109/CDC40024.2019.9030026.

[5] Moritz Diehl, Rachel Leuthold, and Roland (Eds) Schmehl. The international airborne wind energy conference 2017: Book of abstracts. 5-6 October, Freiburg, 2017. ISBN 978-94-6186-846-6. doi: https://doi.org/10.4233/uuid:4c361ef1-d2d2-4d14-9868-16541f60edc7.

[6] Directorate-General for Research ECORYS and Innovation (European Commission). Study on challenges in the commercialisation of airborne wind energy systems, 2018.

[7] B. Etkin. *Dynamics of Atmospheric Flight*. Dover Books on Aeronautical Engineering. Dover Publications, 2012. ISBN 9780486141657.

[8] L. Fagiano. Systems of Tethered Multicopters: Modeling and Control Design. *IFAC PAPERSONLINE*, 50(1):4610–4615, 2017. doi: https://doi.org/10.1016/j.ifacol.2017.08.653. 20th World Congress of the International-Federation-of-Automatic-Control (IFAC), Toulouse, FRANCE, JUL 09-14, 2017.

[9] Uwe Fechner, Rolf van der Vlugt, Edwin Schreuder, and Roland Schmehl. Dynamic model of a pumping kite power system. *Renewable Energy*, 83:705 – 716, 2015. ISSN 0960-1481. doi: http://dx.doi.org/10.1016/j.renene.2015.04.028.

[10] Flavio Gohl and Rolf H. Luchsinger. *Simulation Based Wing Design for Kite Power*, pages 325–338. Springer Berlin Heidelberg, Berlin, Heidelberg, 2013. ISBN 978-3-642-39965-7. doi: https://doi.org/10.1007/978-3-642-39965-7_18.

[11] Sébastien Gros and Moritz Diehl. *Modeling of Airborne Wind Energy Systems in Natural Coordinates*, pages 181–203. Springer Berlin Heidelberg, Berlin, Heidelberg, 2013. ISBN 978-3-642-39965-7. doi: https://doi.org/10.1007/978-3-642-39965-7_10.

[12] W. Hongxun. Chinese kites (traditional chinese arts and culture). In Foreign Languages Press, editor, *Matrix Methods of Structural Analysis*. China Books and Periodicals, 1989.

[13] B. Houska and M. Diehl. Optimal control for power generating kites. In *2007 European Control Conference (ECC)*, pages 3560–3567, 2-5 July 2007, Kos, Greece, July 2007. doi: https://doi.org/10.23919/ECC.2007.7068861.

[14] Zhijie Liu, Jinkun Liu, and Wei He. Modeling and vibration control of a flexible aerial refueling hose with variable lengths and input constraint. *Automatica*, 77:302 – 310, 2017. doi: https://doi.org/10.1016/j.automatica.2016.11.002.

[15] A. Pastor-Rodríguez, G. Sánchez-Arriaga, and M. Sanjurjo-Rivo. Modeling and stability analysis of tethered kites at high-altitudes. *Journal of Guidance, Control, and Dynamics*, 40(8):1892–1901, 2017. doi: https://doi.org/10.2514/1.G002550.

[16] P. Payne and Ch. McCutchen. Self-erecting windmill. united states, patent 3987987, 1976.

[17] A.R. Podgaets and W.J. Ockels. Flight control and stability of a multiple kites tethered system. 9-13 October 2006, Makuhari Messe, Chiba, Japan, 01 2006.

[18] Roderick Read. Kite networks for harvesting airborne wind energy. In R. Schmehl, editor, *Airborne Wind Energy. Green Energy and Technology*, chapter 21, page 515. Springer, Singapore, Oxford, 2018.

[19] G. Sánchez-Arriaga. Dynamics and control of single line kites. *The Aeronautical Journal*, 110(1111): 615–621, 2006. doi: https://doi.org/10.1017/S0001924000001470.

[20] G. Sánchez-Arriaga, M. García-Villalba, and R. Schmehl. Modeling and dynamics of a two-line kite. *Applied Mathematical Modelling*, 47:473 – 486, 2017. doi: https://doi.org/10.1016/j.apm.2017.03.030.

[21] G. Sánchez-Arriaga, A. Pastor-Rodríguez, R. Borobia-Moreno, and R. Schmehl. A constraint-free flight simulator package for airborne wind energy systems. *Journal of Physics: Conference Series*, 1037(6): 062018, 2018. doi: https://doi.org/10.1088/1742-6596/1037/6/062018.

[22] G. Sánchez-Arriaga, A. Pastor-Rodríguez, M. Sanjurjo-Rivo, and R. Schmehl. A lagrangian flight simulator for airborne wind energy systems. *Applied Mathematical Modelling*, 69:665–684, 2019. doi: https://doi.org/10.1016/j.apm.2018.12.016.

[23] Roland (Ed.) Schmehl. *Airborne Wind Energy - Advances in Technology Development and Research*. 03 2018. ISBN 978-981-10-1947-0. doi: https://doi.org/10.1007/978-981-10-1947-0.

[24] E.J. Terink, J. Breukels, R. Schmehl, and W.J. Ockels. Flight dynamics and stability of a tethered inflatable kiteplane. *AIAA Journal of Aircraft*, 48(2):503–513, 2012. doi: https://doi.org/10.2514/1.C031108.

[25] Marco Tognon and Antonio Franchi. Nonlinear observer for the control of bi-tethered multi aerial robots. 2015 IEEE International Conference on Intelligent Robots and Systems, pages 1852–1857, 28 September - 3 October 2015, Hamburg, Germany, 2015. doi: https://doi.org/10.1109/IROS.2015.7353619.

[26] Simon Watson, Alberto Moro, Vera Reis, Charalampos Baniotopoulos, Stephan Barth, Gianni Bartoli, Florian Bauer, Elisa Boelman, Dennis Bosse, Antonello Cherubini, Alessandro Croce, Lorenzo Fagiano, Marco Fontana, Adrian Gambier, Konstantinos Gkoumas, Chris Golightly, Mikel Latour,

Peter Jamieson, John Kaldellis, and Ryan Wiser. Future emerging technologies in the wind power sector: A european perspective. *Renewable and Sustainable Energy Reviews*, 113:109270, 10 2019. doi: https://doi.org/10.1016/j.rser.2019.109270.

[27] P. Williams, B. Lansdorp, and W. Ockels. Optimal crosswind towing and power generation with tethered kites. *Journal of Guidance, Control and Dynamics*, 31(1):81–93, 2008. doi: https://doi.org/10.2514/1.30089.

[28] Mario Zanon, Sebastien Gros, Joel Andersson, and Moritz Diehl. Airborne wind energy based on dual airfoils. *Control Systems Technology, IEEE Transactions on*, 21:1215–1222, 07 2013. doi: https://doi.org/10.1109/TCST.2013.2257781.

View publication stats